

Environmentally Sustainable Synthesis of a $\text{CoFe}_2\text{O}_4\text{-TiO}_2/\text{rGO}$ Ternary Photocatalyst: A Highly Efficient and Stable Photocatalyst for High Production of Hydrogen (Solar Fuel)

Hafeez Yusuf Hafeez,[†] Sandeep Kumar Lakhera,[‡] Naresh Narayanan,^{†,‡} Subramaniam Harish,[§] Yasuhiro Hayakawa,[§] Byeong-Kyu Lee,^{||} and Bernaurdshaw Neppolian^{*,†,||}

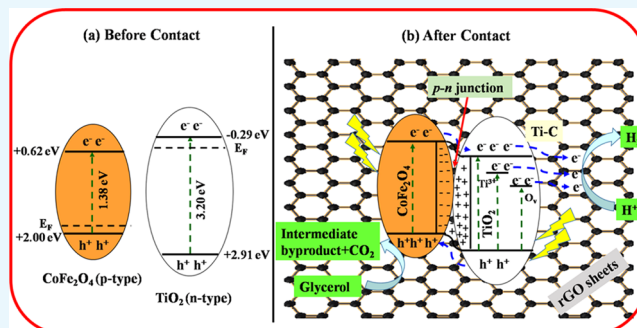
[†]SRM Research Institute and [‡]Department of Physics and Nanotechnology, SRM Institute of Science and Technology, Kattankulathur, Chennai 603203, Tamil Nadu, India

[§]Research Institute of Electronics, Shizuoka University, 3-5-1 Johoku, Naka-Ku, Hamamatsu 432-8011, Japan

^{||}Department of Civil and Environmental Engineering, University of Ulsan (UOU), Daehak-ro 93, Nam-gu, Ulsan 44610, South Korea

Supporting Information

ABSTRACT: Herein, a magnetically separable reduced graphene oxide (rGO)-supported $\text{CoFe}_2\text{O}_4\text{-TiO}_2$ photocatalyst was developed by a simple ultrasound-assisted wet impregnation method for efficient photocatalytic H_2 production. Integration of CoFe_2O_4 with TiO_2 induced the formation of Ti^{3+} sites that remarkably reduced the optical band gap of TiO_2 to 2.80 eV from 3.20 eV. Moreover, the addition of rGO improved the charge carrier separation by forming Ti–C bonds. Importantly, the $\text{CoFe}_2\text{O}_4\text{-TiO}_2/\text{rGO}$ photocatalyst demonstrated significantly enhanced photocatalytic H_2 production compared to that from its individual counterparts such as TiO_2 and $\text{CoFe}_2\text{O}_4\text{-TiO}_2$, respectively. A maximum H_2 production rate of $76\,559\,\mu\text{mol g}^{-1}\text{ h}^{-1}$ was achieved with a 20 wt % CoFe_2O_4 - and 1 wt % rGO-loaded TiO_2 photocatalyst, which was approximately 14-fold enhancement when compared with the bare TiO_2 . An apparent quantum yield of 12.97% at 400 nm was observed for the $\text{CoFe}_2\text{O}_4\text{-TiO}_2/\text{rGO}$ photocatalyst under optimized reaction conditions. This remarkable enhancement can be attributed to synergistically improved charge carrier separation through Ti^{3+} sites and rGO support, viz., Ti–C bonds. The recyclability of the photocatalyst was ascertained over four consecutive cycles, indicating the stability of the photocatalyst. In addition, it is worth mentioning that the photocatalyst could be easily separated after the reaction using a simple magnet. Thus, we believe that this study may open a new way to prepare low-cost, noble-metal-free magnetic materials with TiO_2 for sustainable photocatalytic H_2 production.



1. INTRODUCTION

In response to ever increasing global energy demand and the environmental concerns due to the rapid development and population growth, it becomes necessary and urgent to develop a renewable, clean, cost-effective, and sustainable source of energy.¹ The fossil fuels (coal, oil, and natural gas) remain the main source of energy because of their availability and low cost. However, they have several environmental issues, such as the greenhouse effect, global warming, etc. Moreover, fossil fuel resources are finite, depleted rapidly, and cannot be recovered. Extensive research has been carried out to find alternative sources of energy. One of the most promising options is solar energy conversion into hydrogen energy via the water splitting process.¹ The solar hydrogen production through photocatalytic water splitting is considered as the most viable approach to address the global energy crisis.² Especially, photocatalytic water splitting by employing a photocatalyst has shown a great potential because of its low

cost and clean and highly sustainable future for solar hydrogen evolution. Over the past few decades, designing highly efficient, scalable, and stable photocatalysts for solar water splitting has been a great challenge.^{3,4} Many photocatalysts, such as ZnO , CdS , SnO_2 , $\text{g-C}_3\text{N}_4$, and TiO_2 , are suffering from poor charge carrier separation and transfer, photocorrosion, and photostability, having a band gap in the UV region; therefore, they hinder photocatalysis for commercial viability.^{5–9} Enormous progress has been made to address these problems by doping metal, loading carbon material (reduced graphene oxide (rGO), carbon nanotube (CNT)), and designing heterojunction nanocomposite photocatalysts.^{10,11} Among these, constructing a heterojunction nanocomposite is a promising approach to obtain high-performance photocatalysts.

Received: November 19, 2018

Accepted: December 19, 2018

Published: January 10, 2019

TiO₂ is one of the most efficient and promising photocatalysts for the water-splitting application owing to its nontoxicity, low cost, photoactivity, and high chemical stability.^{12,13} Nevertheless, despite being a good photocatalyst, the low efficiency and the wide band gap (~3.20 eV) of TiO₂ hinder its visible light absorption along with its photocatalytic performance.¹⁴ Furthermore, a high charge carrier recombination also reduces the photocatalytic efficiency of TiO₂. To date, several efforts have been made to overcome such problems; among them, the construction of heterojunction with other photocatalysts and also carbon materials, such as TiO₂-Cu₂O/rGO,¹⁵ g-C₃N₄-TiO₂/rGO,¹⁶ AgI-meso-TiO₂/rGO,¹⁷ MWCT-TiO₂/rGO,¹⁸ CuFe₂O₄-TiO₂/rGO,¹⁹ and Ag₂O-TiO₂,²⁰ has shown efficient charge carrier separation and transfer, resulting in improved photocatalytic performance.

In general, it is a very difficult task to remove or settle the catalyst after the reaction in heterogeneous catalysis. A useful strategy was proposed by integration of a TiO₂-based photocatalyst with magnetic materials such as, CuFe₂O₄, CoFe₂O₄, and so on.^{19,21} In particular, cobalt ferrite (CoFe₂O₄) with a spinel structure has attracted significant attention for a variety of applications including photo-degradation of organic pollutants and water splitting because of its visible-light-responsive photocatalytic activity, low band gap, nontoxicity, corrosion resistance, and chemical stability in aqueous solution, apart from its magnetic property.^{22,23} Chang et al. reported that the CoFe₂O₄@ZnS photocatalyst fabricated for 0.5 h (ZnS growth time) achieved a H₂ production rate of 1650 μmol g⁻¹ h⁻¹.²⁴ Chen et al. also reported that g-C₃N₄ modified with CoFe₂O₄ exhibited almost 3 times increment in H₂ production activity in comparison with pure g-C₃N₄, with an apparent quantum yield of 3.5%.²⁵ However, the low conduction band potential compared with the redox hydrogen potential makes CoFe₂O₄ an inferior photocatalyst toward photocatalytic water splitting, but it can be used as a photosensitizer.^{26,27}

Several attempts have been carried out to improve the photocatalytic performance of metal oxides and ferrites, such as incorporation of graphene, carbon nanotube (CNT), and fullerene.^{15,18,26,27} Graphene is a two-dimensional layer of sp²-hybridized carbon atoms and has become highly attractive in different applications like sensors, supercapacitors, and catalysis because of its unique properties of a high specific surface area and faster carrier mobility.^{28,29} Graphene oxide (GO) is produced through the oxidation of graphite powder and can be reduced to reduced graphene oxide (rGO) by considerably removing the oxygen functional groups (epoxy) using chemical methods.³⁰⁻³² Various reduced graphene oxide (rGO)-based photocatalysts, such as MWCT-TiO₂/rGO,¹⁸ MoS₂-TiO₂/rGO,³³ TiO₂-Cu₂O/rGO,¹⁵ and NS-rGO/TiO₂,³⁴ have been shown to improve the photocatalytic hydrogen production efficiency. This improvement in the photocatalytic activity has been ascribed to the suppression of electron-hole pair recombination and high electron mobility of the rGO.

Recently, Gupta et al. have reported that loading rGO onto the CoFe₂O₄-TiO₂ nanocomposite has shown improvement in the chlorpyrifos degradation activity under visible light.³⁵ However, to the best of our knowledge, there was no report documented in the literature for the hydrogen production application. Herein, we reported, for the first time, the synthesis of a rGO-supported CoFe₂O₄-TiO₂ photocatalyst by the combination of the wet impregnation and ultrasound

methods for the photocatalytic water splitting. The CoFe₂O₄-TiO₂/rGO photocatalysts exhibited exceptional photocatalytic activity in water splitting to generate hydrogen compared with the pure TiO₂ nanoparticles (NPs). It is worth mentioning here that loading CoFe₂O₄ and rGO onto TiO₂ drastically enhanced the H₂ production rate to 76559 μmol g⁻¹ h⁻¹, which is the second among all of the rGO- and TiO₂-based photocatalysts.

2. RESULTS AND DISCUSSION

The X-ray diffraction (XRD) patterns of the prepared pristine TiO₂, CoFe₂O₄, CoFe₂O₄-TiO₂, and CoFe₂O₄-TiO₂/rGO photocatalysts are shown in Figure 1. From the XRD results, it

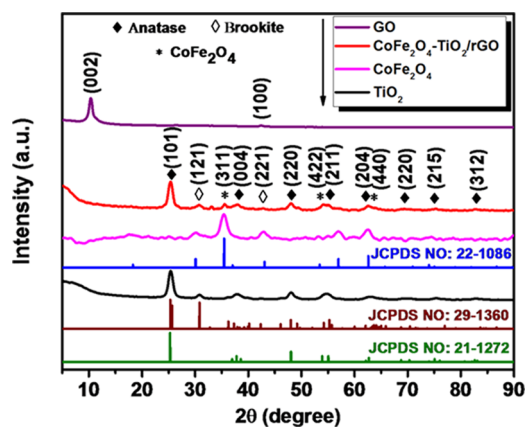


Figure 1. XRD patterns of GO, TiO₂, CoFe₂O₄, and CoFe₂O₄-TiO₂/rGO photocatalysts.

is found that GO exhibits two peaks at $2\theta = 9.8$ and 42.5° , corresponding to the (001) and (002) planes, respectively. The diffraction peaks observed at $2\theta = 18.2, 30.1, 35.5, 37.1, 43.1, 53.4, 56.9,$ and 62.6° correspond to the (111), (220), (311), (222), (400), (422), (511), and (440) crystallographic planes of CoFe₂O₄ (JCPDS Card no. 22-1086), respectively.³⁶ Pristine TiO₂ shows two different phases, i.e., at $25.3, 37.8, 48.0, 53.9, 55.1, 62.7, 69.7, 75.6,$ and 83.0° , which are assigned to the (101), (004), (200), (105), (211), (204), (220), (215) and (312) crystal planes of the anatase phase (JCPDS 21-1272), respectively,³⁷ and at 30.8 and 42.3° , which are assigned to the (121) and (221) crystallographic planes of the brookite phase of TiO₂ (JCPDS 29-1360).³⁸ The weight fraction ratio of the anatase to the brookite phase, according to integrated intensities of the anatase (101) plane at $2\theta = 25.3^\circ$ and the brookite (121) plane at $2\theta = 30.8^\circ$, was found to be ~63:37, which is the benefit of the photocatalyst in improving photocatalytic activity.³⁸ The XRD pattern confirms the presence of multiphases (CoFe₂O₄ and anatase/brookite TiO₂) in the CoFe₂O₄-TiO₂/rGO photocatalyst. However, the peak attributed to the rGO is not visible, possibly due to overlapping with the (101) diffraction peak of anatase TiO₂ or low loading of rGO (1 wt %).³⁹

Figure 2 displays the Fourier transform infrared (FTIR) spectra of GO, CoFe₂O₄, TiO₂, CoFe₂O₄-TiO₂, and CoFe₂O₄-TiO₂/rGO photocatalysts. GO exhibits the characteristic peak at 3432 cm^{-1} , corresponding to the O-H stretching, whereas the peaks appearing at $1715, 1622, 1397, 1233,$ and 1057 cm^{-1} are related to the stretching vibration (C=O), aromatic carbon vibration (C=C), bending in carboxylic and carbonyl (O-H) groups, vibration of epoxy

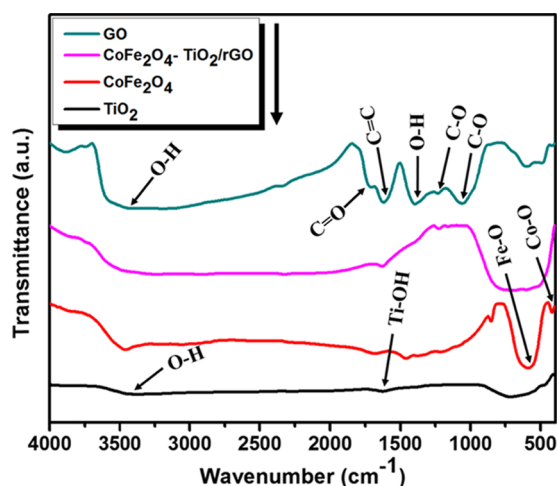


Figure 2. FTIR spectra of GO, TiO₂, CoFe₂O₄, CoFe₂O₄-TiO₂, and CoFe₂O₄-TiO₂/rGO photocatalysts.

groups (C–O), and stretching vibration of alkoxy groups (C–O), respectively.⁴⁰ For pristine TiO₂, the IR peaks observed at 3432, 1626, and 1368 cm⁻¹ can be ascribed to the stretching vibration mode of O–H and bonding modes of Ti–OH and Ti–O, respectively,^{41,42} whereas the broad band at 900–400 cm⁻¹ is related to bulk titanate.⁴³ CoFe₂O₄ NPs show two broad bands at 410 and 586 cm⁻¹, which are assigned to the intrinsic stretching vibrations of the metal at the tetrahedral site and octahedral metal stretching, respectively.^{44,45} The broad band at 400–800 cm⁻¹ observed for CoFe₂O₄-TiO₂/rGO can be ascribed to the Ti–O–Ti, Ti–O–C, or Fe–O stretching vibrations. The peak intensities of GO functional groups are significantly less in CoFe₂O₄-TiO₂/rGO photocatalysts, indicating the reduction of GO during calcination. In the FTIR spectra of the CoFe₂O₄-TiO₂/rGO photocatalyst, all of the IR peaks of both CoFe₂O₄ and TiO₂ are present, which are in accordance with the XRD and X-ray photoelectron spectroscopy (XPS) results.

The Raman spectra of pristine TiO₂, CoFe₂O₄-TiO₂, and CoFe₂O₄-TiO₂/rGO photocatalysts are displayed in Figure 3. Pure TiO₂ shows Raman peaks at about 146, 403, 521, and 640 cm⁻¹ corresponding to the E_g(1), B_{1g}, A_{1g} + B_{1g}(2), and E_g(2)

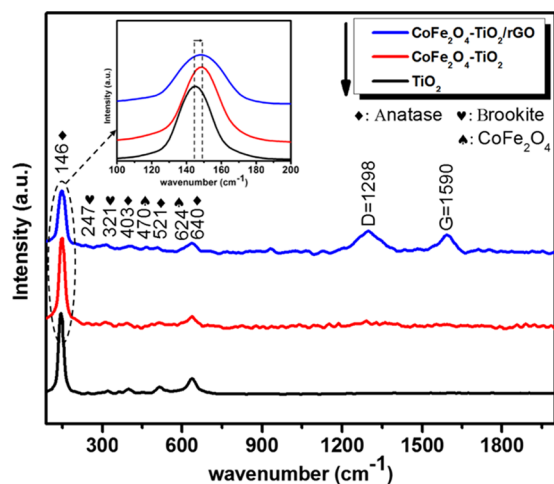


Figure 3. Raman spectra of TiO₂, CoFe₂O₄-TiO₂, and CoFe₂O₄-TiO₂/rGO photocatalysts.

modes of anatase, respectively, whereas the peaks at 247 and 321 cm⁻¹ are related to the A_{1g} and B_{1g} modes of the brookite phase of TiO₂.¹⁶ Additional Raman peaks appearing at 470 cm⁻¹ (T_{1g}(2)) and 624 cm⁻¹ (A_{1g}(2)) in the CoFe₂O₄-TiO₂/rGO photocatalyst can be assigned to the symmetric stretching of the Fe–Co–O bond and the symmetric vibration mode of the metal in the octahedral and tetrahedral sites of CoFe₂O₄, respectively.^{46,47} The Raman peak intensities of TiO₂ decreased in the CoFe₂O₄-TiO₂/rGO photocatalyst, which can be due to the incorporation of CoFe₂O₄ and rGO into TiO₂. As seen in Figure 3 (inset), the E_g(1) mode for CoFe₂O₄-TiO₂ and CoFe₂O₄-TiO₂/rGO photocatalysts is slightly shifted in comparison with the pristine TiO₂, indicating the coupling of rGO and CoFe₂O₄ with TiO₂. In the Raman spectra of the CoFe₂O₄-TiO₂/rGO photocatalyst, two characteristic peaks of graphitic carbon (G-band) and disordered carbon (D-band) were observed at 1590 and 1298 cm⁻¹, respectively. The I_D/I_G ratio of the CoFe₂O₄-TiO₂/rGO photocatalyst is found to be 1.03, which is higher than that of GO (0.93), indicating effective reduction of GO during the thermal process.¹⁷

Figure S1a,b displays the scanning electron microscopy (SEM) images of the pure TiO₂ and CoFe₂O₄-TiO₂/rGO photocatalysts. As seen in Figure S1a,b, TiO₂ exhibits irregular-shaped and agglomerated morphology and CoFe₂O₄ NPs are well dispersed on the surface of TiO₂ NPs, respectively. The purity of the CoFe₂O₄-TiO₂/rGO photocatalyst was verified by the energy-dispersive spectrometry (EDS) spectrum (Figure S1c), and the corresponding wt % results are shown in the table in the inset of Figure S1c. Figure 4 shows the transmission electron microscopy (TEM) images of the CoFe₂O₄-TiO₂/rGO photocatalyst. As seen from the TEM image in Figure 4a, CoFe₂O₄-TiO₂ photocatalysts are well dispersed and anchored on the rGO sheets with an average particle size of 35.2 nm as seen in the inset of Figure 4a. The high-resolution (HR)-TEM image of the CoFe₂O₄-TiO₂/rGO photocatalysts is displayed in Figure 4b, which clearly discloses the interface formation between CoFe₂O₄ and TiO₂. The lattice fringes with *d*-spacings of 0.35 and 0.26 nm correspond to the TiO₂(101) and CoFe₂O₄(311) planes, respectively.³⁴ The corresponding selected area electron diffraction (SAED) patterns of the CoFe₂O₄-TiO₂/rGO photocatalyst are shown in Figure 4c. The diffraction rings could be ascribed to the (121) crystalline plane of brookite, the (101) and (220) planes of the anatase phase TiO₂, and the (311) plane of cobalt ferrite. The SAED patterns further confirm the crystallinity of CoFe₂O₄-TiO₂/rGO photocatalysts, which are in good accordance with the XRD patterns.

Figure 5 displays the absorption and the Tauc plots of the TiO₂, CoFe₂O₄, CoFe₂O₄-TiO₂, and CoFe₂O₄-TiO₂/rGO photocatalysts.⁴⁸ According to Figure 5a, the absorption band of the pristine TiO₂ is at 388 nm, which corresponds to a band gap energy of 3.20 eV (Figure 5b), whereas CoFe₂O₄ with a black surface shows a broad absorption range from 200 to 1000 nm. After loading of 20 wt % CoFe₂O₄, the absorption edge of TiO₂ is red-shifted from 388 to 419 nm with a band gap of 2.96 eV. Similarly, after incorporation 1 wt % rGO, the absorption edge further shifted to 443 nm, corresponding to a band gap of 2.80 eV. It is clear evidence that rGO not only is a solid support but also interacts chemically with the metal (Ti), thereby reducing the band gap energy of TiO₂, which further enhances the charge carrier separation and transfer.^{49,50} The diffuse reflectance spectroscopy (DRS) results clearly show the

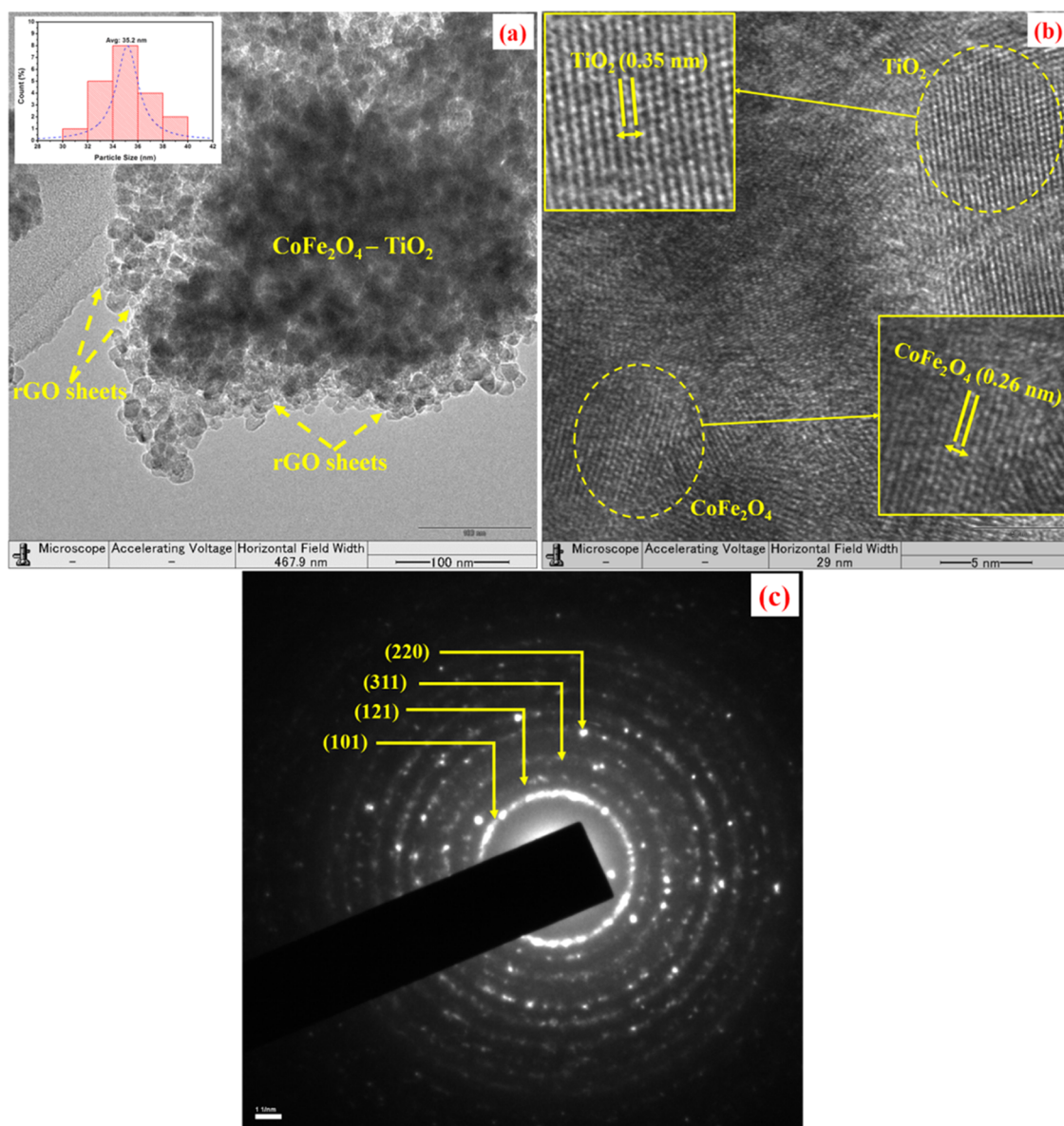


Figure 4. (a) TEM image of the $\text{CoFe}_2\text{O}_4\text{-TiO}_2/\text{rGO}$ photocatalyst, (b) HR-TEM image of the $\text{CoFe}_2\text{O}_4\text{-TiO}_2/\text{rGO}$ photocatalyst, and (c) SAED pattern of the $\text{CoFe}_2\text{O}_4\text{-TiO}_2/\text{rGO}$ photocatalyst.

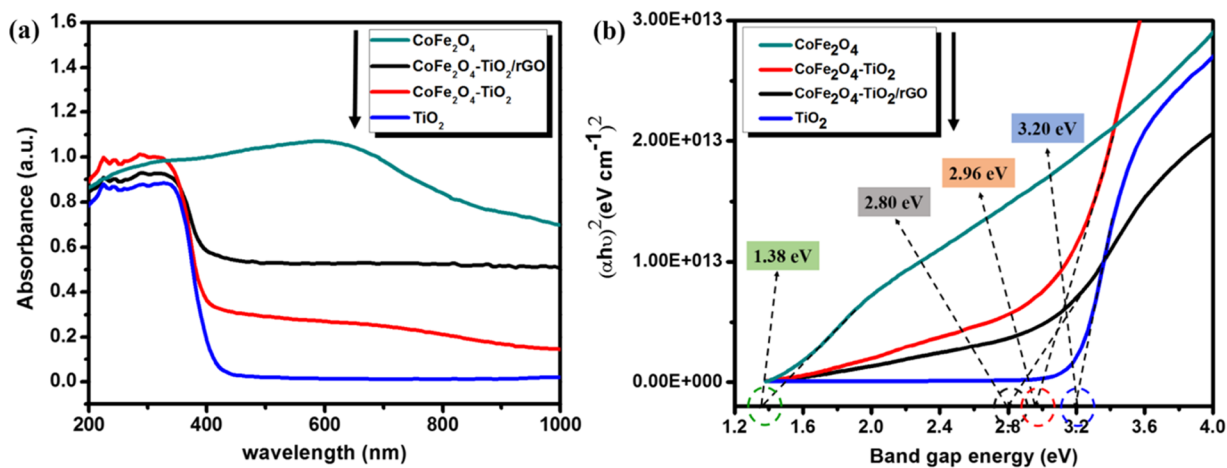


Figure 5. (a) UV-vis diffuse reflectance spectra and (b) Tauc plots of TiO_2 , CoFe_2O_4 , $\text{CoFe}_2\text{O}_4\text{-TiO}_2$, and $\text{CoFe}_2\text{O}_4\text{-TiO}_2/\text{rGO}$ photocatalysts.

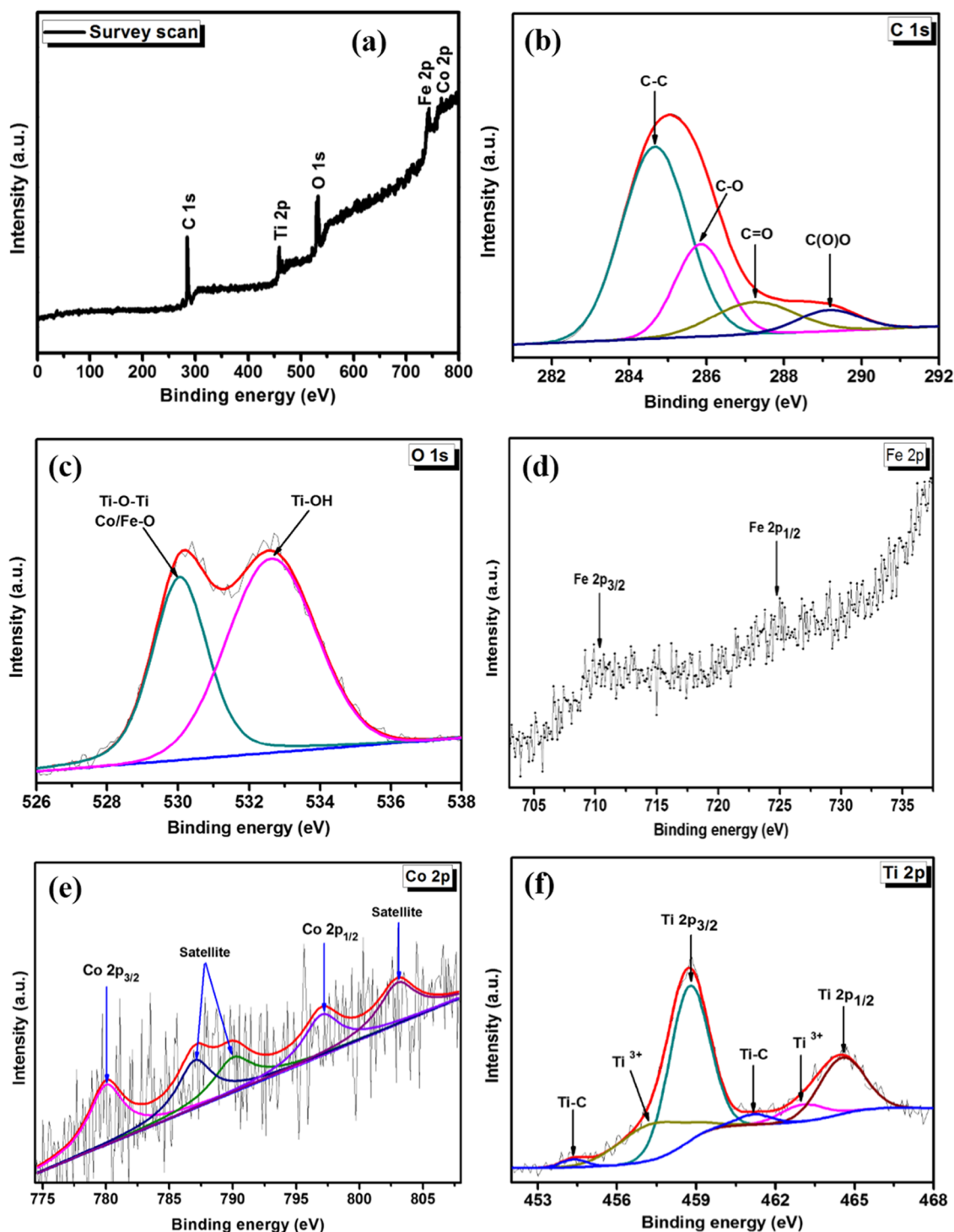


Figure 6. (a) XPS spectra of the $\text{CoFe}_2\text{O}_4\text{-TiO}_2/\text{rGO}$ photocatalyst and the corresponding high-resolution XPS spectra of (b) C 1s (c) O 1s (d) Fe 2p (e) Co 2p, and (f) Ti 2p.

incorporation of CoFe_2O_4 and rGO into TiO_2 shifts the absorption intensity of TiO_2 in the visible region by narrowing the band gap, which results from the formation of defect sites, such as Ti^{3+} and oxygen vacancies (O_v), addition of CoFe_2O_4 and Ti-C bond formation, thereby light absorbance increase, and more efficient utilization of light could be obtained, resulting in an increased photocatalytic performance of TiO_2 .^{49–51}

The chemical and electronic structures of the $\text{CoFe}_2\text{O}_4\text{-TiO}_2/\text{rGO}$ photocatalysts are examined by XPS. The peak

signals for Fe, Co, O, C, and Ti are observed in the survey scan of the $\text{CoFe}_2\text{O}_4\text{-TiO}_2/\text{rGO}$ photocatalysts, as seen in Figure 6a. As shown in Figure 6b, C 1s displays four asymmetric peaks at 284.6, 285.8, 287.3, and 289.2 eV related to the aromatic ring (C=C/C-C), hydroxyl and epoxy groups (C-O), carbonyl groups (C=O), and carboxyl groups (C(O)O), respectively.⁵² The O 1s spectrum (Figure 6c) exhibits peaks at 530.4 and 532.7 eV related to the lattice oxygen in Ti-O-Ti and/or crystal lattice oxygen (oxygen bonded to the metal) in CoFe_2O_4 and oxygen in the Ti-OH bonds, respectively.^{53,54}

Additionally, the Fe 2p spectrum (Figure 6d) shows two peaks, Fe 2p_{3/2} (710.2 eV) and Fe 2p_{1/2} (725.0 eV).⁵⁵ The deconvolution of Co 2p is depicted in Figure 6e. The peaks at 797.0 and 780.1 eV are related to Co 2p_{1/2} and Co 2p_{3/2}, respectively. The main Co 2p_{3/2} peak has two satellite peaks at 786.7 and 790.1 eV, which are ascribed to Co²⁺ in octahedral and tetrahedral sites, respectively. The intense Co 2p_{1/2} satellite peak at 803.0 eV confirms the presence of Co²⁺ species in the photocatalyst.⁵⁶ The XPS spectrum of Ti 2p (Figure 6f) displays two peaks: Ti 2p_{3/2} (458.7 eV) and Ti 2p_{1/2} (464.6 eV).⁵⁷ The peaks appearing at 457.3 and 463.0 eV correspond to the Ti 2p_{3/2} and Ti 2p_{1/2} peaks of Ti³⁺, indicating that Ti³⁺ species were formed as a result of the reaction of free carbon with oxygen in air on the surface of TiO₂, which favors oxygen in the lattice of TiO₂, resulting in the formation of oxygen vacancies (O_v) and the low valence state of Ti³⁺.⁴⁹ Importantly, Ti³⁺ and O_v could act as an electron trapping center, which largely inhibit electron–hole pair recombination, resulting in enhanced photocatalytic activity. Notably, additional peaks appearing at 455.0 and 461.1 eV related to the Ti–C bond were observed, indicating the existence of chemical bonding between TiO₂ and rGO sheets.⁵⁸ The formation of Ti–C bond could also extend light absorption of TiO₂ to the visible region.⁵⁹ The XPS results further revealed the phase purity of the photocatalysts and bonding of rGO and TiO₂ in the photocatalysts.

The photoluminescence (PL) spectra of pure TiO₂, CoFe₂O₄–TiO₂, CoFe₂O₄–TiO₂/rGO photocatalysts are displayed in Figure 7. The PL emission spectra of bare TiO₂

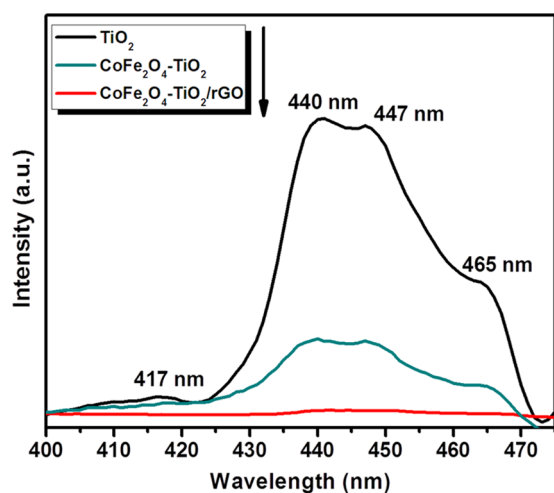


Figure 7. PL spectra of TiO₂, CoFe₂O₄–TiO₂, and CoFe₂O₄–TiO₂/rGO photocatalysts.

show several peaks at 417, 440, 447, and 465 nm. The observed peak at 417 nm is related to the band gap transition, whereas those at 440 and 447 nm are assigned to the defect sites including surface oxygen vacancies (O_v) and Ti³⁺ presence in TiO₂ NPs.^{60–62} The peak at 465 nm is assigned to the free excitation emission of the band gap.⁶⁰ After incorporating CoFe₂O₄ on the TiO₂ surface, the PL emission intensity is significantly reduced, indicating lower charge carrier recombination. Furthermore, a significant PL quenching was observed when rGO was added to CoFe₂O₄–TiO₂ photocatalysts. Indeed, the effect of rGO on the charge carrier separation was phenomenal and also revealed that rGO

hindered or suppressed electron–hole pair recombination, which improved photocatalytic activity.⁴⁹

The electrochemical impedance spectroscopy (EIS) is a promising method that is used to study the charge separation and transfer behavior of a photocatalyst.⁶³ In general, a bigger arc radius of the Nyquist circle indicates a higher charge-transfer resistance. Figure S2 displays the Nyquist circle of TiO₂, CoFe₂O₄–TiO₂, and CoFe₂O₄–TiO₂/rGO photocatalysts measured under simulated solar light irradiation. The larger arc radius for TiO₂ suggests a higher charge-transfer resistance compared to that of CoFe₂O₄–TiO₂ and CoFe₂O₄–TiO₂/rGO photocatalysts. As shown in Figure S2, the CoFe₂O₄–TiO₂/rGO ternary photocatalyst exhibited a smaller arc radius than that of CoFe₂O₄–TiO₂.^{64,65} The results indicated that loading rGO significantly improved the electron mobility, thereby suppressing the charge-transfer resistance. This result is in accordance with the above PL results. Figure S3 shows the photocurrent study of TiO₂, CoFe₂O₄–TiO₂, and CoFe₂O₄–TiO₂/rGO photocatalysts. The CoFe₂O₄–TiO₂/rGO ternary photocatalyst gave higher photocurrent response compared to that of bare TiO₂ and CoFe₂O₄–TiO₂. This higher photocurrent response produced by the CoFe₂O₄–TiO₂/rGO photocatalyst can be related to the high electron mobility of rGO at the interfaces of the CoFe₂O₄ and TiO₂ heterojunction that greatly enhances migration and efficient charge carrier separation, which is in accordance with PL and EIS studies. These results are also consistent with the previous studies reported by Babu and Jiang et al.^{15,66}

The magnetic separation performance of the prepared photocatalysts was further studied. Figure 8 displays the

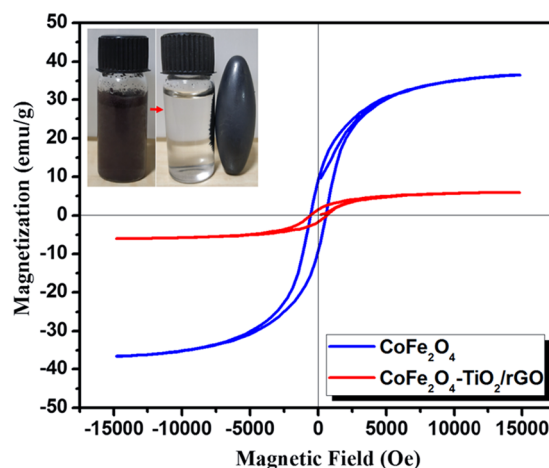


Figure 8. Magnetic hysteresis loop of CoFe₂O₄ and CoFe₂O₄–TiO₂/rGO photocatalysts.

magnetic hysteresis loop of CoFe₂O₄ and CoFe₂O₄–TiO₂/rGO photocatalysts, in which CoFe₂O₄ shows a symmetric hysteresis loop with a higher magnetization saturation value of ~36.5 emu g^{−1} compared to that of the CoFe₂O₄–TiO₂/rGO photocatalyst (~5.9 emu g^{−1}). This low magnetization saturation value is related to the presence of the nonmagnetic TiO₂ and rGO. It still can be separated from the reaction solution using a simple magnet as seen in the inset of Figure 8. Furthermore, Figure 8 (inset) clearly reveals that the CoFe₂O₄–TiO₂/rGO photocatalyst retains its magnetic separation performance after four consecutive cycles and can be a promising magnetic photocatalyst material. The above

results demonstrated that the $\text{CoFe}_2\text{O}_4\text{-TiO}_2/\text{rGO}$ photocatalyst has good stability and recyclability during the photocatalytic reaction.

The photocatalytic H_2 production activities of prepared photocatalysts were determined for water splitting under UV–vis light irradiation with glycerol as a hole scavenger. As depicted in Figure 9, the relative order of H_2 production for

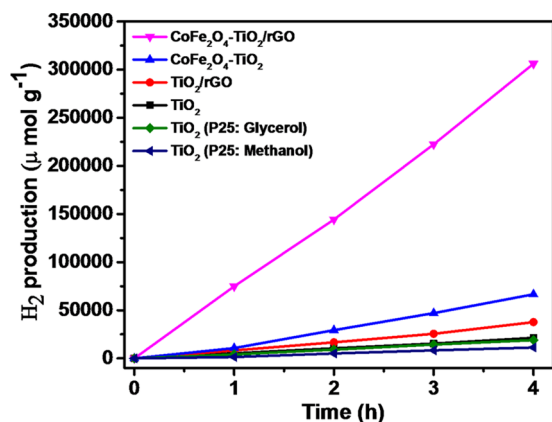


Figure 9. Photocatalytic H_2 evolution of as-prepared TiO_2 , TiO_2 (P25: Glycerol), TiO_2 (P25: Methanol), rGO/TiO_2 , $\text{CoFe}_2\text{O}_4\text{-TiO}_2$, and $\text{CoFe}_2\text{O}_4\text{-TiO}_2/\text{rGO}$ photocatalysts.

the photocatalysts is P-25 TiO_2 (methanol, $2772 \mu\text{mol g}^{-1} \text{h}^{-1}$) < P-25 TiO_2 (glycerol, $4739 \mu\text{mol g}^{-1} \text{h}^{-1}$) < TiO_2 ($5336 \mu\text{mol g}^{-1} \text{h}^{-1}$) < rGO/TiO_2 ($9421 \mu\text{mol g}^{-1} \text{h}^{-1}$) < $\text{CoFe}_2\text{O}_4\text{-TiO}_2$ ($16\,673 \mu\text{mol g}^{-1} \text{h}^{-1}$) < $\text{CoFe}_2\text{O}_4\text{-TiO}_2/\text{rGO}$ ($76\,559 \mu\text{mol g}^{-1} \text{h}^{-1}$). The photocatalytic H_2 production rate achieved using present TiO_2 NPs was 1.13 and 1.92 times higher than that of the commercially available TiO_2 Degussa P-25 using glycerol and methanol, respectively. Moreover, the ternary $\text{CoFe}_2\text{O}_4\text{-TiO}_2/\text{rGO}$ photocatalyst exhibits almost 8-fold increment of H_2 production activity compared to that of the binary TiO_2/rGO photocatalyst (Figure 9). To understand the effects of CoFe_2O_4 loading on hydrogen production, different wt % of CoFe_2O_4 (10, 20, 30, and 40 wt %) were loaded onto TiO_2 , resulting in an increased H_2 production activity till 20 wt %, which then decreases. The optimized sample (20 wt %) produced $16\,673 \mu\text{mol g}^{-1} \text{h}^{-1}$ hydrogen (Figure 10), which is almost 3-fold higher than that from the bare TiO_2 . As shown in Figure 11, rGO plays a prominent role in boosting the H_2 production activity of the as-prepared photocatalysts. After incorporation of different wt % of rGO (0.5, 1.0, 2.0, and 3.0 wt %) in the $\text{CoFe}_2\text{O}_4\text{-TiO}_2$ photocatalyst, a further enhancement in the H_2 evolution rate is observed (Figure 11). Surprisingly, a remarkable photocatalytic H_2 production rate of $76\,559 \mu\text{mol g}^{-1} \text{h}^{-1}$ is achieved with the optimized 1.0 wt % rGO in $\text{CoFe}_2\text{O}_4\text{-TiO}_2$ that exceeds 14.4-folds higher than that of the bare TiO_2 . An apparent quantum yield of 12.97% at 400 nm was observed for the $\text{CoFe}_2\text{O}_4\text{-TiO}_2/\text{rGO}$ photocatalyst under optimized reaction conditions. This superior photocatalytic performance of the $\text{CoFe}_2\text{O}_4\text{-TiO}_2/\text{rGO}$ photocatalyst is associated with the existence of defect sites (Ti^{3+} and O_v), Ti-C bond formation, and effective formation of heterojunction between CoFe_2O_4 and TiO_2 , which efficiently facilitate the rapid interfacial charge transfer in the presence of rGO matrix.^{49,58} Furthermore, the photocatalytic H_2 evolution achieved in the present study is significantly higher than already reported results, as depicted in

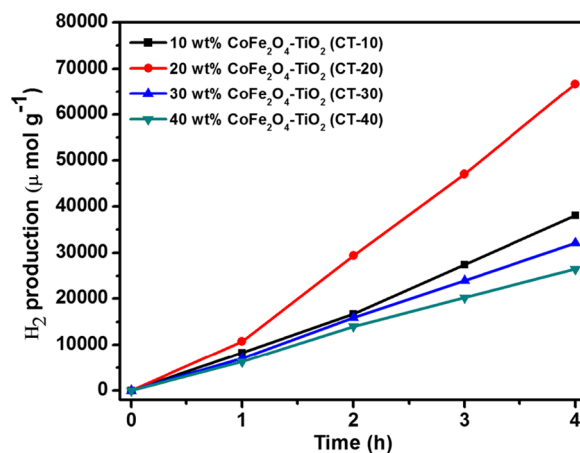


Figure 10. Photocatalytic H_2 evolution of as-prepared 10 wt % $\text{CoFe}_2\text{O}_4\text{-TiO}_2$ (CT-10), 20 wt % $\text{CoFe}_2\text{O}_4\text{-TiO}_2$ (CT-20), 30 wt % $\text{CoFe}_2\text{O}_4\text{-TiO}_2$ (CT-30), and 40 wt % $\text{CoFe}_2\text{O}_4\text{-TiO}_2$ (CT-40) photocatalysts.

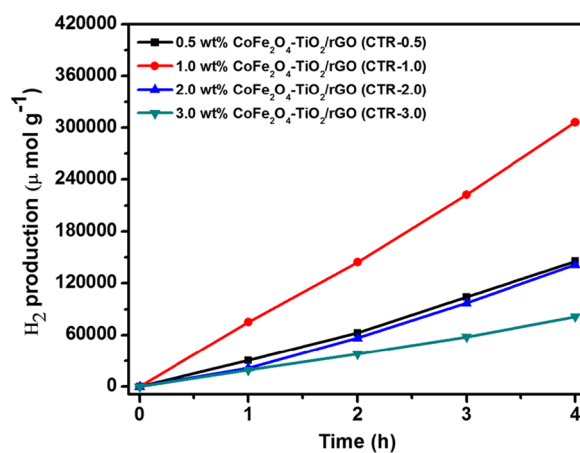


Figure 11. Photocatalytic H_2 evolution of as-prepared 0.5 wt % $\text{CoFe}_2\text{O}_4\text{-TiO}_2/\text{rGO}$ (CTR-0.5), 1 wt % $\text{CoFe}_2\text{O}_4\text{-TiO}_2/\text{rGO}$ (CTR-1), 2 wt % $\text{CoFe}_2\text{O}_4\text{-TiO}_2/\text{rGO}$ (CTR-2), and 3 wt % $\text{CoFe}_2\text{O}_4\text{-TiO}_2/\text{rGO}$ (CTR-3) photocatalysts.

Table S1. To determine the recyclability and durability of the optimized $\text{CoFe}_2\text{O}_4\text{-TiO}_2/\text{rGO}$ photocatalyst, four consecutive cycles of photocatalytic reaction were carried out. Each cycle was performed for 4 h under UV–visible irradiation. At the end of every cycle, the reactor solution was entirely wrapped with an aluminum foil and kept overnight in the dark. The reactor solution was evacuated, purged with N_2 gas, and then placed on a magnetic stirrer under UV–visible irradiation for another reaction. A similar trend was followed up to four cycles. No significant loss of photocatalytic activity was observed for the $\text{CoFe}_2\text{O}_4\text{-TiO}_2/\text{rGO}$ photocatalyst up to four cycles, as shown in Figure 12. A minor decrease in the photocatalytic activity in the fourth cycle is observed, which can be attributed to a decrease of glycerol concentration in the solution because of the decomposition of glycerol.

The improved photocatalytic performance of the as-prepared $\text{CoFe}_2\text{O}_4\text{-TiO}_2/\text{rGO}$ photocatalyst can be attributed to the combination of visible light sensitization, formation of a p–n heterojunction, presence of defect sites (Ti^{3+} and O_v), and synergistic effect of the rGO support layer. Based on the above results, it is undoubtedly proved that the formation of a p–n heterojunction, defect sites, and rGO support is the

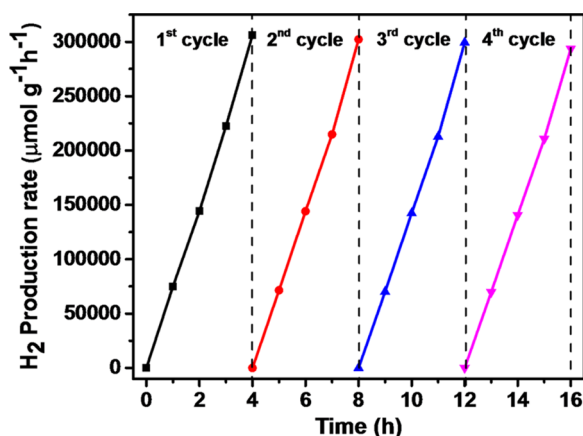


Figure 12. Reusability of the CoFe₂O₄-TiO₂/rGO photocatalyst for four run cycles.

important factor to enhance the photocatalytic performance of the photocatalyst. The conduction band (E_{CB}) and valence band (E_{VB}) positions of the photocatalysts were computed theoretically by the following empirical formulas (eqs 1 and 2)^{67,68}

$$E_{CB} = \chi - E^c - 0.5E_g \quad (1)$$

$$E_{VB} = E_g - E_{VB} \quad (2)$$

where E_{CB} and E_{VB} represent the conduction and valence band potentials of a photocatalyst, respectively. χ is the electronegativity of the photocatalyst (the χ values for CoFe₂O₄ and TiO₂ are 5.81 and 5.81 eV, respectively^{69,70}), E^c represents the energy of free electrons on the hydrogen scale (~4.5 eV), and E_g stands for the band-gap energy of the photocatalyst. Thus, the band-gap energies of TiO₂ and CoFe₂O₄ were found to be 3.20 and 1.38 eV, respectively (Figure 5b). Table 1 shows the calculated values of E_{VB} and E_{CB} for CoFe₂O₄ and TiO₂ using eqs 1 and 2, respectively.

Table 1. Electronegativity, Band Gap, and Conduction Band and Valence Band Positions of the Photocatalysts on NHE

photocatalyst	χ (eV)	E_g (eV)	E_{CB} (eV)	E_{VB} (eV)
CoFe ₂ O ₄	5.81	1.38	+0.62	+2.00
TiO ₂	5.81	3.20	-0.29	+2.91

To understand the charge-transfer mechanism of TiO₂ and CoFe₂O₄ over the rGO-supported photocatalyst, a plausible energy-level diagram for the CoFe₂O₄-TiO₂/rGO photocatalyst system is constructed, as depicted in Figure 13. On the normal hydrogen electrode (NHE), the E_{CB} edges of TiO₂ and CoFe₂O₄ were calculated to be -0.29 and +0.62, respectively, and the corresponding E_{VB} edges are at +2.91 and +2.00 eV, respectively (Table 1). The Fermi level (E_F) of n-type TiO₂ is below E_{CB} , whereas that of p-type CoFe₂O₄ is above E_{VB} .⁷¹ Before contact, the E_{CB} position of TiO₂ is higher than that of CoFe₂O₄ and the E_F of TiO₂ is above that of CoFe₂O₄, as depicted in Figure 13a. When these two photocatalysts are in contact, the E_F of CoFe₂O₄ moves up, whereas the E_F of TiO₂ moves down, until the E_F 's of TiO₂ and CoFe₂O₄ get the same value. A p-n heterojunction is formed at the interface, and the electron transfer occurs from CoFe₂O₄ to TiO₂ until it reached thermal equilibrium, resulting in the formation of the space charge region. The TiO₂ and CoFe₂O₄ bands do bend, and the

whole energy level of CoFe₂O₄ rises, whereas that of TiO₂ descends.^{72,73} As a result, the E_{CB} position of CoFe₂O₄ is higher than that of TiO₂. Hence, the electrons can easily transfer from E_{CB} of CoFe₂O₄ to E_{CB} of TiO₂ because of band bending. It was reported previously that the existence of Ti³⁺ and O_v induced new localized states below the CB of TiO₂, which is responsible for the decrease of band gap of TiO₂.^{74,75} The excess electrons accumulated in the E_{CB} of TiO₂ and the electrons present in the defect sites (Ti³⁺ and O_v) are mediated via the rGO surface and reduce protons (H⁺) to produce H₂, as shown in Figure 13b.^{49,74} Therefore, the formed defect sites (Ti³⁺ and O_v) substantially suppress the charge carrier recombination rate and extend the visible light absorption, thereby enhancing the H₂ production efficiency.⁷⁶ The photogenerated holes can easily transfer from the higher E_{VB} of TiO₂ (+2.91 eV) to the lower E_{VB} of CoFe₂O₄ (+2.00 eV), where they do react with glycerol to generate an intermediate product and CO₂. Thus, this providential increase in hydrogen production performance can be related to the presence of defect sites (Ti³⁺ and O_v) and Ti-C bond formation, which efficiently extend the photoresponse of TiO₂ to the visible region.

3. CONCLUSIONS

In summary, a magnetic material CoFe₂O₄ and TiO₂ photocatalysts along with reduced graphene oxide (rGO) as a support were prepared by a simple ultrasound-assisted wet impregnation method. A superior hydrogen production activity was achieved for the optimized magnetic material CoFe₂O₄ (20 wt %) and rGO (1 wt %) loaded on the TiO₂ surface. The effect of rGO loading was phenomenal in the present study and exhibited maximum H₂ production rate of 76 559 μmol g⁻¹ h⁻¹, which is ~5- and ~14-fold enhancement compared to that of CoFe₂O₄-TiO₂ and the bare TiO₂, respectively. This remarkable enhancement was related to the addition of CoFe₂O₄, presence of defect sites (Ti³⁺ and O_v), and strong interaction between rGO sheets and TiO₂ through Ti-C bond formation, which were responsible for the synergistic effect. The XPS and PL studies undoubtedly proved the existence of defect sites (Ti³⁺ and O_v) and Ti-C bond in the CoFe₂O₄-TiO₂/rGO photocatalysts. Furthermore, a substantial reduction in PL emission intensity and the high transient photocurrent response further supported high transfer efficiency and the charge carrier separation in the presence of rGO sheet, resulting in the superior photocatalytic activity. Moreover, the photocatalyst showed good stability and can easily be separated after the reaction using a simple magnet.

4. EXPERIMENTAL DETAILS

4.1. Materials. Graphite powder (99.9995%) and cobalt nitrate hexahydrate and iron nitrate nonahydrate, citric acid, and graphite powder were procured from Alfa Aesar and Merck, India, respectively. Titanium tetraisopropoxide (TTIP) and commercially available solvents such as ethanol, methanol, and isopropanol were purchased from Sigma-Aldrich, SRL and Rankem, India, respectively.

4.2. Characterization Studies. The crystal phase of the as-synthesized photocatalysts was analyzed by X-ray diffraction (PANalytical X'pert powder diffractometer) using Cu K α radiation ($\lambda = 1.5406 \text{ \AA}$). The morphologies of the photocatalysts were recorded on a transmission electron microscope (TEM, JEOL JEM 2100F, accelerating voltage of

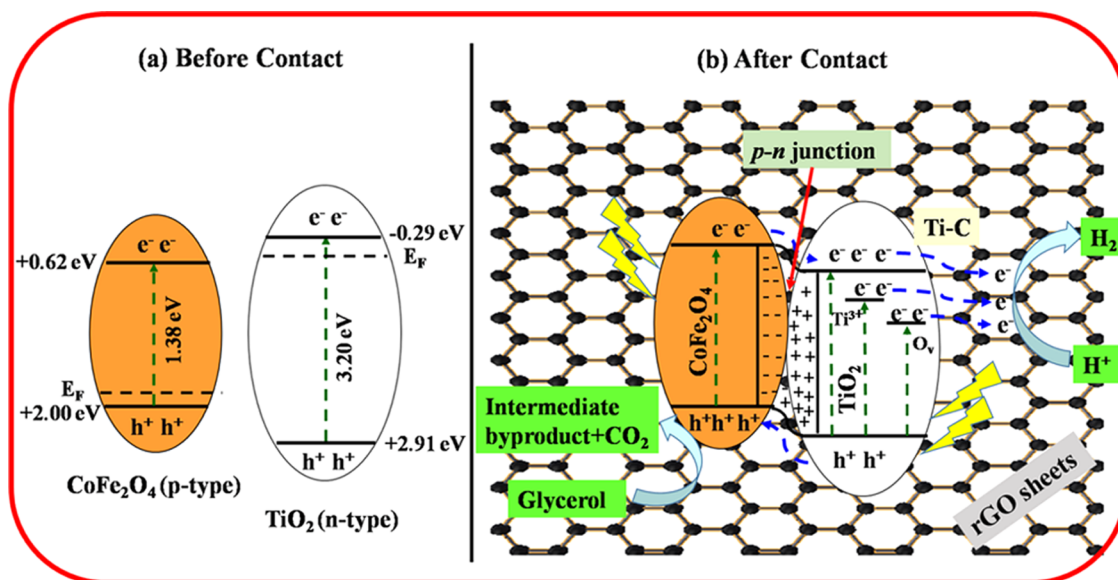
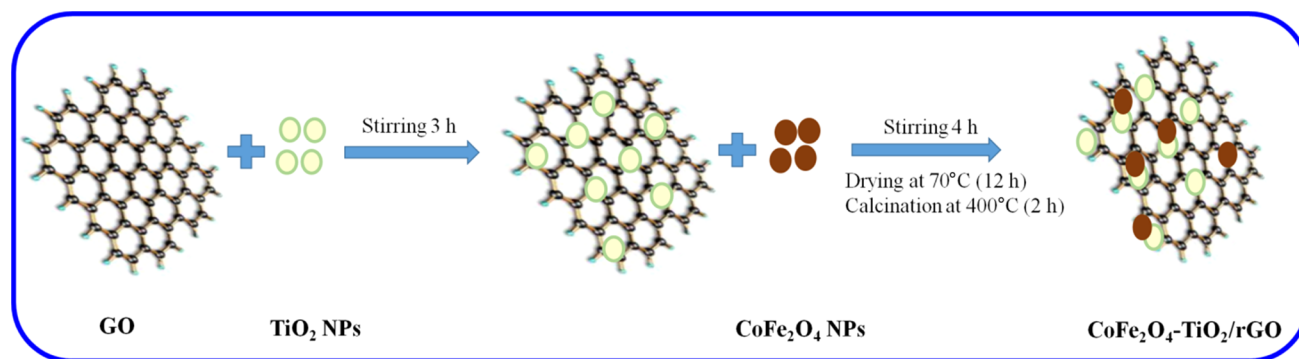


Figure 13. Plausible mechanism of photocatalytic activity under UV-vis light irradiation of the $\text{CoFe}_2\text{O}_4\text{-TiO}_2/\text{rGO}$ photocatalyst.

Scheme 1



200 kV). HR-TEM was used to record the size and shape of the as-synthesized photocatalysts. Field emission-scanning electron microscopy images were obtained using a FEI Quanta FEG 200 HR-SEM. UV-vis diffuse reflectance spectroscopy (DRS) measurements were performed with a Shimadzu UV-2600 UV-vis spectrophotometer in DRS mode. The chemical and elemental compositions of the photocatalyst were identified by X-ray photoelectron spectroscopy (XPS) using Al $K\alpha$ instruments, as a source at 1350 eV. Fourier transform infrared (FTIR) spectroscopy was performed using a Perkin Elmer spectrometer. Raman spectra were examined by Bruker IFS 66V/FRA 106. Photoluminescence (PL) spectra of photocatalysts were analyzed by a JASCO FP-6300 fluorescence spectrometer.

4.3. Fabrication of the $\text{CoFe}_2\text{O}_4\text{-TiO}_2/\text{rGO}$ Photocatalyst. **4.3.1. Synthesis of TiO_2 NPs.** In typical synthesis, TiO_2 NPs were prepared as reported previously.¹⁶ Isopropanol (15 mL) and titanium tetraisopropoxide (5 mL) were slowly added into 250 mL of deionized (DI) water at pH \sim 3, under vigorous stirring, respectively. A white precipitate was formed, which was stirred for another 2 h and then kept in the oven for 22 h at 60 °C. The precipitate was collected and centrifuged seven times with DI water. The resultant sample was dried overnight at 80 °C followed by calcination for 2 h at 400 °C. The photocatalyst was labeled as Ti.

4.3.2. Synthesis of CoFe_2O_4 NPs. CoFe_2O_4 NPs were prepared via the precipitation method.⁷⁷ In a typical synthesis, $\text{Fe}(\text{NO}_3)_3 \cdot 9\text{H}_2\text{O}$ (2.0 g) and $\text{Co}(\text{NO}_3)_2 \cdot 6\text{H}_2\text{O}$ (0.73 g) were put into a glass beaker with 50 mL of deionized (DI) water. The mixture was dissolved after stirring for 10 min and, separately, citric acid (1.44 g) was dissolved in 50 mL of DI water. Then, the above solution was mixed and sonicated for 20 min followed by vigorous stirring for 3 h. The pH was maintained at 9 by adding dilute NaOH. A brown precipitate was formed, which was further stirred for 3 h at 80 °C. A dark brown gel was collected, which was centrifuged five times with DI water, dried overnight at 70 °C, and then calcined at 550 °C for 2 h. The photocatalyst was labeled as CF.

4.3.3. Synthesis of $\text{CoFe}_2\text{O}_4\text{-TiO}_2/\text{rGO}$ Photocatalysts. GO was prepared through a modified Hummer's method as reported in a previous report.¹⁵ The $\text{CoFe}_2\text{O}_4\text{-TiO}_2/\text{rGO}$ photocatalyst was fabricated by the ultrasound-assisted wet impregnation method, as shown in Scheme 1. Different amounts of GO (0.5, 1.0, 2.0, and 3.0 wt %) were added to a beaker containing the ethanol-water mixture. Then, the solution was sonicated for 1 h followed by addition of TiO_2 under stirring for 3 h. A different weight percentage of CoFe_2O_4 (10, 20, 30, and 40 wt %) was loaded onto the above solution under vigorous stirring for 4 h. Finally, the samples were washed five times with DI water and dried at 70 °C for 12 h, followed by calcination for 2 h at 400 °C. The samples were

labeled as CTR-0.5, CTR-1, CTR-2, and CTR-3. The same trend was adopted to synthesize the CoFe_2O_4 - TiO_2 photocatalyst without GO, and the photocatalysts were labeled as CT-10, CT-20, CT-30, and CT-40.

4.4. Hydrogen Production Test. The photocatalytic H_2 production experiment was carried out in a glass reactor (135 mL) closed with a rubber septum. A xenon lamp (250 W) was used as a light source. Then, 5.0 mg of photocatalyst was added into 50 mL of glycerol–water (5/45 v/v) solution. The mixture was magnetically stirred in the dark under N_2 purging for 30 min to ensure adsorption–desorption equilibrium. Then, the sample solution was irradiated under the light source. The H_2 gas produced was evaluated using a gas chromatograph (Shimadzu GC-2014; nitrogen as a carrier gas). The apparent quantum efficiency (AQY) of the prepared photocatalyst was calculated as shown in Section S1.

4.5. Photoelectrochemical Studies. All of the electrochemical measurements were performed in an electrochemical workstation (CHI608E) using the traditional three-electrode experimental system: glassy carbon electrode (area 0.385 mm^2), Pt, and Ag/AgCl were utilized as the working, counter, and the reference electrodes, respectively. A 300 W xenon lamp (OSRAM, Germany) was employed as the source of light, and 0.5 M Na_2SO_4 aqueous solution as an electrolyte. Then, 2.5 mg of the photocatalyst was dispersed in 250 μL of ethanol and 5 μL of Nafion and then ultrasonicated for 1 h to form a slurry solution. The slurry was dip-coated onto a pre-cleaned working electrode. After air-drying, the prepared photoelectrode was immersed in a 0.5 M Na_2SO_4 electrolyte solution.

■ ASSOCIATED CONTENT

Supporting Information

The Supporting Information is available free of charge on the ACS Publications website at DOI: 10.1021/acsomega.8b03221.

Details on apparent quantum efficiency (AQY %) calculation, SEM and EDS images of the photocatalysts, EIS measurements and photocurrent studies of the prepared photocatalysts, and the comparison table of the photocatalytic H_2 production activity with existing TiO_2 -based materials (PDF)

■ AUTHOR INFORMATION

Corresponding Author

*E-mail: neppolian.b@res.srmuniv.ac.in. Phone: +91-44-2741-7916. Fax: +91-44-2745-6702.

ORCID

Byeong-Kyu Lee: 0000-0003-2851-3206

Bernaerdshaw Neppolian: 0000-0002-8508-8771

Notes

The authors declare no competing financial interest.

■ ACKNOWLEDGMENTS

The authors express sincere thanks to the Ministry of New and Renewable Energy (MNRE), New Delhi, India (103/239/2015-NT), and the Science and Engineering Research Board Department of Science and Technology (SERB-DST), New Delhi, India (EMR/2014/000645).

■ REFERENCES

- (1) Zeng, D.; Xu, W.; Ong, W.-J.; Xu, J.; Ren, H.; Chen, Y.; Zheng, H.; Peng, D.-L. Toward noble-metal-free visible-light-driven photocatalytic hydrogen evolution: Monodisperse sub-15 nm Ni_2P nanoparticles anchored on porous g- C_3N_4 nanosheets to engineer 0D-2D heterojunction interfaces. *Appl. Catal., B* **2018**, *221*, 47–55.
- (2) Wang, S.; Guan, B. Y.; Wang, X.; Lou, X. W. D. Formation of Hierarchical Co_9S_8 @ ZnIn_2S_4 Heterostructured Cages as An Efficient Photocatalyst for Hydrogen Evolution. *J. Am. Chem. Soc.* **2018**, *140*, 15145–15148.
- (3) Chen, X.; Shen, S.; Guo, L.; Mao, S. S. Semiconductor-based photocatalytic hydrogen generation. *Chem. Rev.* **2010**, *110*, 6503–6570.
- (4) Kudo, A.; Miseki, Y. Heterogeneous photocatalyst materials for water splitting. *Chem. Soc. Rev.* **2009**, *38*, 253–278.
- (5) Liu, H.; Zhu, D.; Shi, H.; Shao, X. Fabrication of a Contamination-Free Interface between Graphene and TiO_2 Single Crystals. *ACS Omega* **2016**, *1*, 168–176.
- (6) Lu, X.; Wang, G.; Xie, S.; Shi, J.; Li, W.; Tong, Y.; Li, Y. Efficient photocatalytic hydrogen evolution over hydrogenated ZnO nanorod arrays. *Chem. Commun.* **2012**, *48*, 7717–7719.
- (7) Li, Y.; Hu, Y.; Peng, S.; Lu, G.; Li, S. Synthesis of CdS nanorods by an ethylenediamine assisted hydrothermal method for photocatalytic hydrogen evolution. *J. Phys. Chem. C* **2009**, *113*, 9352–9358.
- (8) Lin, Z.; Wang, X. Nanostructure Engineering and Doping of Conjugated Carbon Nitride Semiconductors for Hydrogen Photosynthesis. *Angew. Chem., Int. Ed.* **2013**, *52*, 1735–1738.
- (9) Zhu, T.; Wu, H. B.; Wang, Y.; Xu, R.; Lou, X. W. D. Formation of 1D Hierarchical Structures Composed of Ni_3S_2 Nanosheets on CNTs Backbone for Supercapacitors and Photocatalytic H_2 Production. *Adv. Energy Mater.* **2012**, *2*, 1497–1502.
- (10) Quan, Q.; Xie, S.; Weng, B.; Wang, Y.; Xu, Y.-J. Revealing the Double-Edged Sword Role of Graphene on Boosted Charge Transfer versus Active Site Control in TiO_2 Nanotube Arrays@RGO/ MoS_2 Heterostructure. *Small* **2018**, No. 1704531.
- (11) Xiang, Q.; Yu, J.; Jaroniec, M. Graphene-based semiconductor photocatalysts. *Chem. Soc. Rev.* **2012**, *41*, 782–796.
- (12) Xiang, Q.; Yu, J.; Jaroniec, M. Enhanced photocatalytic H_2 -production activity of graphene-modified titania nanosheets. *Nano-scale* **2011**, *3*, 3670.
- (13) Wu, M.; Gu, L.; Wang, Q.; Wang, C.; Zhang, H. Interfacial assembly of robust TiO_2 nanosheets onto silica-modified reduced graphene oxide for high-efficient degradation of organic dyes. *ChemNanoMat* **2018**, *4*, 387–393.
- (14) Bian, S.; Zhou, C.; Li, P.; Liu, J.; Dong, X.; Xi, F. Graphene quantum dots decorated titania nanosheets heterojunction: efficient charge separation and enhanced visible light photocatalytic performance. *ChemCatChem* **2017**, *9*, 3349–3357.
- (15) Babu, S. G.; Vinoth, R.; Kumar, D. P.; Shankar, M. V.; Chou, H. L.; Vinodgopal, K.; Neppolian, B. Influence of electron storing, transferring and shuttling assets of reduced graphene oxide at the interfacial copper doped TiO_2 p–n heterojunction for increased hydrogen production. *Nanoscale* **2015**, *7*, 7849–7857.
- (16) Hafeez, H. Y.; Lakhera, S. K.; Bellamkonda, S.; Rao, G. R.; Shankar, M. V.; Bahnemann, D. W.; Neppolian, B. Construction of ternary hybrid layered reduced graphene oxide supported g- C_3N_4 - TiO_2 nanocomposite and its photocatalytic hydrogen production activity. *Int. J. Hydrogen Energy* **2018**, *43*, 3892–3904.
- (17) Vinoth, R.; Karthik, P.; Muthamizhchelvan, C.; Neppolian, B.; Ashokkumar, M. Carrier separation and charge transport characteristics of reduced graphene oxide supported visible-light active photocatalysts. *Phys. Chem. Chem. Phys.* **2016**, *18*, 5179–5191.
- (18) Bellamkonda, S.; Thangavel, N.; Hafeez, H. Y.; Neppolian, B.; Rao, G. R. Highly active and stable multi-walled carbon nanotubes-graphene- TiO_2 nanohybrid: An efficient non-noble metal photocatalyst for water splitting. *Catal. Today* **2019**, *321–322*, 120–127.
- (19) Hafeez, H. Y.; Lakhera, S. K.; Karthik, P.; Anpo, M.; Neppolian, B. Facile construction of ternary CuFe_2O_4 - TiO_2 nanocomposite

supported reduced graphene oxide (rGO) photocatalysts for the efficient Hydrogen production. *Appl. Surf. Sci.* **2018**, *449*, 772–779.

(20) Kumar, D. P.; Reddy, N. L.; Karthik, M.; Neppolian, B.; Madhavan, J.; Shankar, M. V. Cu₂O-sensitized TiO₂ nanorods with nano cavities for highly efficient photocatalytic hydrogen production under solar irradiation. *Sol. Energy Mater. Sol. Cells* **2016**, *154*, 78–87.

(21) Ghosh, B. K.; Moitra, D.; Chandel, M.; Ghosh, N. N. Preparation of TiO₂/Cobalt Ferrite/Reduced Graphene Oxide Nanocomposite Based Magnetically Separable Catalyst with Improved Photocatalytic Activity. *J. Nanosci. Nanotechnol.* **2017**, *17*, 4694–4703.

(22) Huang, S.; Xu, Y.; Xie, M.; Xu, H.; He, M.; Xia, J.; Huang, L.; Li, H. Synthesis of magnetic CoFe₂O₄/g-C₃N₄ composite and its enhancement of photocatalytic ability under visible-light. *Colloids Surf., A* **2015**, *478*, 71–80.

(23) Li, N. W.; Zheng, M. B.; Chang, X. F.; Ji, G. B.; Lu, H. L.; Xue, L. P.; Pan, L. J.; Cao, J. M. Preparation of magnetic CoFe₂O₄-functionalized graphene sheets via a facile hydrothermal method and their adsorption properties. *J. Solid State Chem.* **2011**, *184*, 953–958.

(24) Chang, C. J.; Lee, Z.; Chu, K. W.; Wei, Y. H. CoFe₂O₄@ZnS core-shell spheres as magnetically recyclable photocatalysts for hydrogen production. *J. Taiwan Inst. Chem. Eng.* **2016**, *66*, 386–393.

(25) Chen, J.; Zhao, D.; Diao, Z.; Wang, M.; Shen, S. Ferrite boosting photocatalytic hydrogen evolution over graphitic carbon nitride: a case study of (Co, Ni)Fe₂O₄ modification. *Sci. Bull.* **2016**, *61*, 292–301.

(26) Haw, C.; Chiu, W.; Rahman, S. A.; Khiew, P.; Radiman, S.; Shukor, R. A.; Hamid, M. A. A.; Ghazali, N. The design of new magnetic-photocatalyst nanocomposites (CoFe₂O₄-TiO₂) as smart nanomaterials for recyclable-photocatalysis applications. *New J. Chem.* **2016**, *40*, 1124–1136.

(27) He, G.; Ding, J.; Zhang, J.; Hao, Q.; Chen, H. One-Step Ball-Milling Preparation of Highly Photocatalytic Active CoFe₂O₄-Reduced Graphene Oxide Heterojunctions for Organic Dye Removal. *Ind. Eng. Chem. Res.* **2015**, *54*, 2862–2867.

(28) Alamelu, K.; Raja, V.; Shiamala, L.; Ali, B. M. J. Biphasic TiO₂ nanoparticles decorated graphene nanosheets for visible light driven photocatalytic degradation of organic dyes. *Appl. Surf. Sci.* **2018**, *430*, 145–154.

(29) Wen, L.; Spyridon, Z. A Brief Review of the Synthesis and Catalytic Applications of Graphene-Coated Oxides. *ChemCatChem* **2017**, *9*, 2432–2442.

(30) Park, S.; Ruoff, R. S. Chemical methods for the production of graphenes. *Nat. Nanotechnol.* **2009**, *4*, 217–224.

(31) Park, J.; Jin, T.; Liu, C.; Li, G.; Yan, M. Three-Dimensional Graphene-TiO₂ Nanocomposite Photocatalyst Synthesized by Covalent Attachment. *ACS Omega* **2016**, *1*, 351–356.

(32) Chua, C. K.; Pumera, M. Chemical Reduction of Graphene Oxide: a Synthetic Chemistry Viewpoint. *Chem. Soc. Rev.* **2014**, *43*, 291–312.

(33) Xiang, Q.; Yu, J.; Jaroniec, M. Synergetic effect of MoS₂ and graphene as cocatalysts for enhanced photocatalytic H₂ production activity of TiO₂ nanoparticles. *J. Am. Chem. Soc.* **2012**, *134*, 6575–6578.

(34) Chen, D.; Zou, L.; Li, S.; Zheng, F. Nanospherical like reduced graphene oxide decorated TiO₂ nanoparticles: an advanced catalyst for the hydrogen evolution reaction. *Sci. Rep.* **2016**, *6*, No. 20335.

(35) Gupta, V. K.; Eren, T.; Atar, N.; Yola, M. L.; Parlak, C.; Karimi-Maleh, H. CoFe₂O₄@TiO₂ decorated reduced graphene oxide nanocomposite for photocatalytic degradation of chlorpyrifos. *J. Mol. Liq.* **2015**, *208*, 122–129.

(36) Niu, Y.; Huang, X.; Zhao, L.; Hu, W.; Li, C. M. One-Pot Synthesis of Co/CoFe₂O₄ Nanoparticles Supported on N-Doped Graphene for Efficient Bifunctional Oxygen Electrocatalysis. *ACS Sustainable Chem. Eng.* **2018**, *6*, 3556–3564.

(37) Neppolian, B.; Wang, Q.; Yamashita, H.; Choi, H. Synthesis and characterization of ZrO₂-TiO₂ binary oxide semiconductor nanoparticles: application and interparticle electron transfer process. *Appl. Catal., A* **2007**, *333*, 264–271.

(38) An, X.; Hu, C.; Liu, H.; Qu, J. Oxygen vacancy mediated construction of anatase/brookite heterophase junctions for high-efficiency photocatalytic hydrogen evolution. *J. Mater. Chem. A* **2017**, *5*, 24989–24994.

(39) Yang, M. Q.; Zhang, N.; Xu, Y. J. Synthesis of Fullerene-, Carbon Nanotube-, and Graphene-TiO₂ Nanocomposite Photocatalysts for Selective Oxidation: A Comparative Study. *ACS Appl. Mater. Interfaces* **2013**, *5*, 1156–1164.

(40) Bose, S.; Kuila, T.; Uddin, M. E.; Kim, N. H.; Lau, A. K. T.; Lee, J. H. In-situ synthesis and characterization of electrically conductive polypyrrole/graphene nanocomposites. *Polymer* **2010**, *51*, 5921–5928.

(41) Abazović, N. D.; Čomor, M. I.; Dramićanin, M. D.; Jovanović, D. J.; Ahrenkiel, S. P.; Nedeljković, J. M. Photoluminescence of Anatase and Rutile TiO₂ Particles. *J. Phys. Chem. B* **2006**, *110*, 25366–25370.

(42) Mugundan, S.; Rajamannan, B.; Viruthagiri, G.; Shanmugam, N.; Gobi, R.; Praveen, P. Synthesis and characterization of undoped and cobalt-doped TiO₂ nanoparticles via sol-gel technique. *Appl. Nanosci.* **2015**, *5*, 449–456.

(43) Kumar, P. M.; Badrinarayanan, S.; Sastry, M. Nanocrystalline TiO₂ studied by optical, FTIR and X-ray photoelectron spectroscopy: correlation to presence of surface states. *Thin Solid Films* **2000**, *358*, 122–130.

(44) Baykal, A.; Kasapoğlu, N.; Köseoğlu, Y.; Başaran, A.; Kavas, H.; Toprak, M. Microwave-induced combustion synthesis and characterization of Ni_xCo_{1-x}Fe₂O₄ nanocrystals (x = 0.0, 0.4, 0.6, 0.8, 1.0). *Cent. Eur. J. Chem.* **2008**, *6*, 125–130.

(45) Patil, S. A.; Mahajan, V. C.; Ghatage, A. K.; Lotke, S. D. Structure and magnetic properties of Cd and Ti/Si substituted cobalt ferrites. *Mater. Chem. Phys.* **1998**, *57*, 86–92.

(46) Ayyappan, S.; Mahadevan, S.; Chandramohan, P.; Srinivasan, M. P.; Philip, J.; Raj, B. Influence of Co²⁺ Ion Concentration on the Size, Magnetic Properties, and Purity of CoFe₂O₄ Spinel Ferrite Nanoparticles. *J. Phys. Chem. C* **2010**, *114*, 6334–6341.

(47) Shemer, G.; Tirosh, E.; Livneh, T.; Markovich, G. Tuning a Colloidal Synthesis to Control Co²⁺ Doping in Ferrite Nanocrystals. *J. Phys. Chem. C* **2007**, *111*, 14334–14338.

(48) Yan, X.; Wang, X.; Gu, W.; Wu, M.; et al. Single 4 crystalline AgIn(MoO₄)₂ Nanosheets Grafted Ag/AgBr Composites with Enhanced Plasmonic Photocatalytic Activity for Degradation of Tetracycline under Visible Light. *Appl. Catal., B* **2015**, *164*, 297–304.

(49) Zhang, Q.; Bao, B.; Wang, X.; Hu, X.; Miao, X.; Chaker, M.; Ma, D. Advanced fabrication of Chemically Bonded Graphene/TiO₂ continuous Fibers with Enhanced Broadband Photocatalytic Properties and Involved Mechanisms Exploration. *Sci. Rep.* **2016**, *6*, No. 38066.

(50) Zhang, H.; Lv, X.; Li, Y.; Wang, Y.; Li, J. P25-Graphene Composite as a High Performance Photocatalyst. *ACS Nano* **2010**, *4*, 380–386.

(51) Zhang, Y.; Pan, C. TiO₂/graphene composite from thermal reaction of graphene oxide and its photocatalytic activity in visible light. *J. Mater. Sci.* **2011**, *46*, 2622–2626.

(52) Dreyer, D. R.; Park, S.; Bielawski, C. W.; Ruoff, R. S. The chemistry of graphene oxide. *Chem. Soc. Rev.* **2010**, *39*, 228–240.

(53) Bian, W. Y.; Yang, Z. R.; Strasser, P.; Yang, R. Z. A CoFe₂O₄/graphene nanohybrid as an efficient bi-functional electrocatalyst for oxygen reduction and oxygen evolution. *J. Power Sources* **2014**, *250*, 196–203.

(54) Luciu, I.; Bartali, R.; Laidani, N. Influence of hydrogen addition to an Ar plasma on the structural properties of TiO_{2-x} thin films deposited by RF sputtering. *J. Phys. D: Appl. Phys.* **2012**, *45*, No. 345302.

(55) Yamashita, T.; Hayes, P. Analysis of XPS spectra of Fe²⁺ and Fe³⁺ ions in oxide materials. *Appl. Surf. Sci.* **2008**, *254*, 2441–2449.

(56) Zong, M.; Huang, Y.; Zhang, N. Reduced graphene oxide-CoFe₂O₄ composite: Synthesis and electromagnetic absorption properties. *Appl. Surf. Sci.* **2015**, *345*, 272–278.

- (57) Chai, B. B.; Peng, T. Y.; Zeng, P.; Mao, J. Synthesis of floriated In_2S_3 decorated with TiO_2 nanoparticles for efficient photocatalytic hydrogen production under visible light. *J. Mater. Chem.* **2011**, *21*, 14587–14593.
- (58) Huang, Q.; Tian, S.; Zeng, D.; Wang, X.; Song, W.; Li, Y.; Xiao, W.; Xie, C. Enhanced photocatalytic activity of chemically bonded TiO_2 /Graphene composites based on the effective interfacial charge transfer through the C–Ti bond. *ACS Catal.* **2013**, *3*, 1477–1485.
- (59) Zhao, D.; Sheng, G.; Chen, C.; Wang, X. Enhanced photocatalytic degradation of methylene blue under visible irradiation on graphene@ TiO_2 dyade structure. *Appl. Catal., B* **2012**, *111–112*, 303–308.
- (60) Liu, B.; Wang, X.; Cai, G.; Wen, L.; Song, Y.; Zhao, X. Low temperature fabrication of Vdoped TiO_2 nanoparticles, structure and photocatalytic studies. *J. Hazard. Mater.* **2009**, *169*, 1112–1118.
- (61) Chen, S. F.; Li, J. P.; Qian, K.; Xu, W. P.; Lu, Y.; Huang, W. X.; Yu, S. H. Large scale photochemical synthesis of $\text{M}@\text{TiO}_2$ nanocomposites ($\text{M} = \text{Ag}, \text{Pd}, \text{Au}, \text{Pt}$) and their optical properties, CO oxidation performance, and antibacterial effect. *Nano Res.* **2010**, *3*, 244–255.
- (62) Zhu, P.; Nair, A. S.; Shengjie, P.; Shengyuan, Y.; Ramakrishna, S. Facile Fabrication of TiO_2 –Graphene composite with enhanced photovoltaic and photocatalytic properties by Electrospinning. *ACS Appl. Mater. Interfaces* **2012**, *4*, 581–585.
- (63) Banerjee, S.; Mohapatra, S. K.; Das, P. P.; Misra, M. Synthesis of Coupled Semiconductor by Filling 1D TiO_2 Nanotubes with CdS. *Chem. Mater.* **2008**, *20*, 6784–6791.
- (64) Wang, S.; Guan, B. Y.; Lou, X. W. Construction of ZnIn_2S_4 - In_2O_3 Hierarchical Tubular Heterostructures for Efficient CO_2 Photoreduction. *J. Am. Chem. Soc.* **2018**, *140*, 5037–5040.
- (65) Jiang, Q.; Sun, L.; Bi, J.; Liang, S.; Li, L.; Yu, Y.; Wu, L. MoS_2 quantum dots modified covalent triazine-based frameworks for enhanced photocatalytic hydrogen evolution. *ChemSusChem* **2018**, *11*, 1108–1113.
- (66) Wang, M.; Liu, Q.; Xu, N.; Su, N.; Wang, X.; Su, W. An amorphous CoS_x modified $\text{Mn}_{0.5}\text{Cd}_{0.5}\text{S}$ solid solution with enhanced visible-light photocatalytic H_2 -production activity. *Catal. Sci. Technol.* **2018**, *8*, 4122–4128.
- (67) Lakhera, S. K.; Watts, A.; Hafeez, H. Y.; Neppolian, B. Interparticle double charge transfer mechanism of heterojunction α - Fe_2O_3 / Cu_2O mixed oxide catalysts and its visible light photocatalytic activity. *Catal. Today* **2018**, *300*, 58–70.
- (68) Lakhera, S. K.; Hafeez, H. Y.; Veluswamy, P.; Ganesh, V.; Khan, A.; Ikeda, H.; Neppolian, B. Enhanced photocatalytic degradation and hydrogen production activity of in situ grown TiO_2 coupled NiTiO_3 nanocomposites. *Appl. Surf. Sci.* **2018**, *449*, 790–798.
- (69) Xu, Y.; Schoonen, M. A. A. The absolute energy positions of conduction and valence bands of selected semiconducting minerals. *Am. Mineral.* **2000**, *85*, 543–556.
- (70) Zhang, L.; Zhang, A.; Lu, H.; Sun, Z.; Sheng, W.; Sun, L.; Xiang, J. Magnetically separable AgI – $\text{BiOI}/\text{CoFe}_2\text{O}_4$ hybrid composites for HgO removal: characterization, activity and mechanism. *RSC Adv.* **2017**, *7*, 31448–31456.
- (71) Zhang, Y.; Schultz, A. M.; Salvador, P. A.; Rohrer, G. S. Spatially selective visible light photocatalytic activity of TiO_2 / BiFeO_3 heterostructures. *J. Mater. Chem.* **2011**, *21*, 4168–4174.
- (72) Humayun, M.; Zada, A.; Li, Z.; Xie, M.; Zhang, X.; Qu, Y.; Raziq, F.; Jing, L. Enhanced visible-light activities of porous BiFeO_3 by coupling with nanocrystalline TiO_2 and mechanism. *Appl. Catal., B* **2016**, *180*, 219–226.
- (73) Xiang, Y.; Ju, P.; Wang, Y.; Sun, Y.; Zhang, D.; Yu, J. Chemical etching preparation of the Bi_2WO_6 / BiOI p–n heterojunction with enhanced photocatalytic antifouling activity under visible light irradiation. *Chem. Eng. J.* **2016**, *288*, 264–275.
- (74) Qiu, B.; Zhou, Y.; Ma, Y.; Yang, X.; Sheng, W.; Xing, M.; Zhang, J. Facile synthesis of the Ti^{3+} self-doped TiO_2 -graphene nanosheet composites with enhanced photocatalysis. *Sci. Rep.* **2015**, *5*, No. 8591.
- (75) Zuo, F.; Bozhilov, K.; Dillon, R. J.; Wang, L.; Smith, P.; Zhao, X.; Bardeen, C.; Feng, P. Active facets on Titanium (III)-Doped TiO_2 : An effective strategy to improve the visible-light photocatalytic Activity. *Angew. Chem.* **2012**, *124*, 6327–6330.
- (76) Karthik, P.; Balaraman, E.; Neppolian, B. Efficient solar light driven H_2 production: A post-synthetic encapsulation of Cu_2O cocatalyst on metal-organic framework (MOF) for boosting the effective charge-carrier separation. *Catal. Sci. Technol.* **2018**, *8*, 3286–3294.
- (77) Sivagurunathan, P.; Gibin, S. R. Preparation and characterization of nanosized cobalt ferrite particles by co-precipitation method with citrate as chelating agent. *J. Mater. Sci.: Mater. Electron.* **2016**, *27*, 8891–8898.